

MatSpectNet: Material Segmentation Network with Domain-Aware and Physically-Constrained Hyperspectral Reconstruction

Anonymous submission

Abstract

Achieving accurate material segmentation for 3-channel RGB images is challenging due to the considerable variation in a material's appearance. Hyperspectral images, which are sets of spectral measurements sampled at multiple wavelengths, theoretically offer distinct information for material identification, as variations in intensity of electromagnetic radiation reflected by a surface depend on the material composition of a scene. However, existing hyperspectral datasets are impoverished regarding the number of images and material categories for the dense material segmentation task, and collecting and annotating hyperspectral images with a spectral camera is prohibitively expensive. To address this, we propose a new model, the MatSpectNet to segment materials with recovered hyperspectral images from RGB images. The network leverages the principles of colour perception in modern cameras to constrain the reconstructed hyperspectral images and employs the domain adaptation method to generalise the hyperspectral reconstruction capability from a spectral recovery dataset to material segmentation datasets. The reconstructed hyperspectral images are further filtered using learned response curves and enhanced with human perception. The performance of MatSpectNet is evaluated on the LMD dataset as well as the OpenSurfaces dataset. Our experiments demonstrate that MatSpectNet attains a 1.60% increase in average pixel accuracy and a 3.42% improvement in mean class accuracy compared with the most recent publication. The project code is attached to the supplementary material and will be published on GitHub.

Introduction

Material segmentation aims to identify the material category of each pixel in the image. Although recent studies indicate that it is possible to achieve acceptable performance with annotated RGB datasets (Heng et al. 2022b,a; Schwartz 2018; Schwartz and Nishino 2020; Bell et al. 2015), the experiments in (Liang et al. 2022; Mao et al. 2022) show that additional measurements of light such as near infra-red and laser beam reflection can distinguish materials more robustly. The theory is that the spectral profile of reflected electromagnetic waves is unique to various materials (Saragadam and Sankaranarayanan 2020; Lichtman and Conchello 2005; Colthup, Daly, and Wiberley 1990). Since spectral cameras (Behmann et al. 2018) can capture the spectral profile of surface materials, it is feasible to use the hyperspectral images they produce for material segmentation.

While hyperspectral imaging has been widely used in geoscience and remote sensing (Zhong et al. 2016; Kalman and Bassett III 1997; Li et al. 2022b; Xue et al. 2021; Mehta et al. 2021; Liu et al. 2019) over twenty years, the cost of collecting hyperspectral images hinders its widespread adoption in material segmentation for daily scenes (Stuart et al. 2022). A spectral camera can take a long acquisition time to scan a megapixel hyperspectral image with sufficient signal-noise ratio since the same amount of light has to be sampled at hundreds of wavelength bands (Behmann et al. 2018; Zhang et al. 2019). This problem necessitates concessions in image spatial and spectral resolution. In addition, the ambient light should be able to cover the entire operating spectrum range, so the spectral camera should be used under daylight or halogen-based illumination. Before taking the hyperspectral images, the camera has to be calibrated with the measurement of black and white reference samples to analyse the material reliably (Behmann et al. 2018; Shaikh et al. 2021). The stringent lighting requirements further restrict the application of hyperspectral images in indoor and motion scenes.

In order to make spectral information more accessible for computer vision applications, researchers have been working on recovering spectral information from more easily obtainable data sources, such as RGB images (Arad et al. 2022). Over the past three years, several methods (Li, Huang, and Zhang 2020; Hu et al. 2022; Cai et al. 2022b) have successfully improved the accuracy of reconstructed hyperspectral images. However, it remains unclear how these methods generalise to images captured by different camera models, as this aspect has not been explicitly investigated. In consideration of this problem, this paper proposes a novel Material Hyperspectral Network (MatSpectNet) to enhance the quality of recovered hyperspectral images on material datasets lacking RGB-hyperspectral image pairs. Figure 1 shows that the proposed MatSpectNet consists of two main sections. The network first learns to recover the hyperspectral images with the physical model of the camera, which serves as a constraint to ensure that the hyperspectral images preserve their physical property that the hyperspectral images can be transformed to RGB images with the physical camera model. Then the recovered hyperspectral images are processed with a multi-layer perceptron (MLP) to learn the material features from the spectral infor-

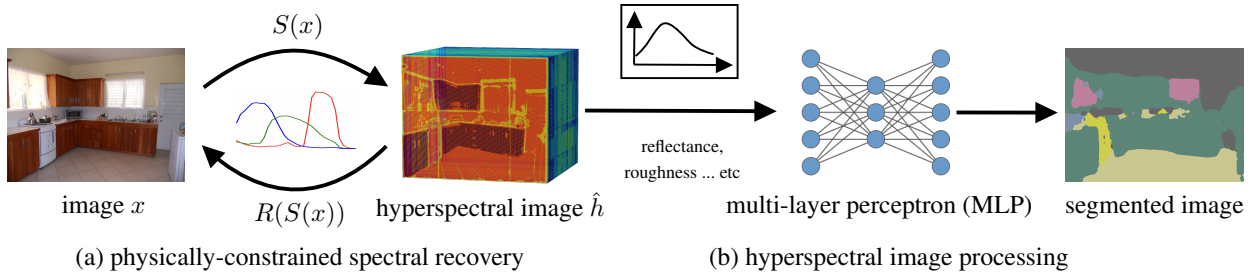


Figure 1: Overall architecture of the proposed MatSpectNet. It consists of two main sections: (a) Recovery of the hyperspectral image from the RGB image, utilising the physical model of the camera. (b) Material feature extraction from the spectra channel using both trainable filters and observations.

mation at each pixel.

To understand the proposed approach, it would be useful to delve into image theory first. An image is the quantitative measurement of the radiation from an illumination source or reflected by scene elements. Similar to the human perception system, the RGB camera measures the radiance of the visible spectrum with red, green and blue spectral response functions that accumulate the electromagnetic radiation from 380 to 720 nanometers and produce the raw-RGB values for each pixel (Magnusson et al. 2020). The raw-RGB image is further processed with in-camera transformations including brightness adjustment and gamma correction to produce the final sRGB image, which is the format commonly used in vision datasets.

Our proposed MatSpectNet model incorporates the physical relationship between hyperspectral and RGB images based on the image theory. Specifically, we exploit the fact that recovered hyperspectral images can be transformed into the original RGB counterparts through known spectral response functions and in-camera processing. This physical constraint is a key feature of our model and enables us to make reliable material predictions based on the recovered hyperspectral images.

However, for open-access material segmentation datasets such as LMD (Schwartz and Nishino 2020) and OpenSurfaces (Bell et al. 2013), the spectral response functions and in-camera image-processing pipeline are unknown. To bring hyperspectral images to the material segmentation task, the MatSpectNet models the physical camera with the sRGB transformation network $R(h)$ that contains trainable components to adjust the unknown parameters. As illustrated in Figure 1, given an sRGB image x , the MatSpectNet optimises that $R(S(x)) = x$ where $S(x)$ is the spectral recovery network that recovers hyperspectral images from sRGB ones. In practice, $S(x)$ is pre-trained on the ARAD_1K dataset (Arad et al. 2022) and fine-tuned together with material datasets. To align the data distribution, the idea of domain adaptation is used during training (Wu et al. 2021).

The recovered hyperspectral images are further processed with learned spectral response filters followed by a MLP to extract per-pixel material features. The spectral response filter is similar to the RGB spectral response functions in the mechanism, which aggregates the spectral information based on the sensitivity to the spectrum at each wavelength.

The per-pixel material features are then tagged with the surface properties such as specularity and roughness queried from the most similar spectral measurement in the spectraldb dataset (Jakubiec 2022), which serves as a piece of additional evidence to identify the materials.

The key contributions of this work are summarised as follows:

1. *Physically-Constrained Spectral Recovery.* Based on the theory that sRGB values can be obtained from hyperspectral images with known spectral response functions and in-camera processing, we propose to regulate the spectral recovery network with a trainable sRGB transformation.
2. *Domain-Aware Network Training.* To leverage the spectral recovery dataset for material segmentation, the domain adaptation is used to alleviate data distribution discrepancy between spectral recovery and material datasets. Moreover, domain-specific spectral response functions and image-processing pipelines are constructed.
3. *Interpretable Hyperspectral Processing.* The learned spectral filters aggregate the spectra across the bandwidth and infer the electromagnetic frequency that contributes to material segmentation most.
4. *Multi-Modal Fused Material Segmentation.* The filtered per-pixel spectra and queried surface properties are fused together to make the material prediction from both spectral measurements as well as other empirical observations (Jain et al. 2013; Jakubiec 2016; Jones and Reinhard 2017; Lucas et al. 2014).

The proposed network, MatSpectNet, outperforms existing models in the material segmentation task. With a per-pixel accuracy (Pixel Acc) of 88.24% and a mean-class accuracy (Mean Acc) of 83.82%, our network shows an improvement of 1.60%/3.42% over the most recent publication (Heng et al. 2022a). Notably, MatSpectNet is particularly adept at recognising material categories that have limited samples, even under varying light conditions. These results are supported by per-category performance metrics and visualised segmentation results.

Background

Material Segmentation

The main challenge in material segmentation is the lack of reliable visual clues in RGB images to distinguish materials. Recent studies have attempted to address this issue by forcing the network to learn material features from cropped image patches, assuming that the absence of object contours can prevent the network from converging to object characteristics such as shape (Heng et al. 2022b,a; Schwartz and Nishino 2020, 2016). However, these implicit methods are designed to learn local features that may improve material segmentation accuracy rather than extracting features that can accurately describe materials. Our proposed MatSpectNet takes a different approach by explicitly exploring material features from hyperspectral images, which quantitatively describe the reflection of light at tens of wavelengths for the surface materials. This approach can identify materials accurately, leading to improved segmentation performance. The justification for using hyperspectral images for material segmentation is in Section C.5 in the supplementary material.

Material Property Measurements

Unlike the properties of objects, which are often associated with appearance semantics like shape and colour, the properties of materials are defined by how they interact with light at their surface and require specialised equipment for measurement. Portable measurement devices such as Time-of-Flight (ToF) cameras (Su et al. 2016) and hyperspectral cameras (Behmann et al. 2018) have the capability to assess the reflective or scattering properties of materials. ToF cameras operate as indirect sensors by determining the elapsed time for a light pulse to travel from the camera to the material and back (Su et al. 2016), while hyperspectral cameras directly capture the spectral signature, which quantifies how much light can be reflected by the material at sampled wavelengths. For material segmentation, hyperspectral cameras are preferred due to their ability to capture a complete scene and provide a comprehensive measurement of material properties through their spectral profiles. Additionally, the spectral profile can facilitate a correlation between measurements obtained from hyperspectral cameras and spectrophotometers (introduced in the supplementary material) provided that the measurements from the hyperspectral camera are lighting invariant.

In addition to sensor-based measurements, human perception also plays a crucial role in evaluating material properties. For instance, the photopic reflectance $V(\lambda)$ and melanopic reflectance $M(\lambda)$ are derived from the measured spectral profile based on the human visual system. The photopic reflectance captures the average human response to the brightness of light in the visible spectrum (Smith and Pokorny 1996), while the melanopic reflectance provides information about the effect of reflected light on the activity of melanopsin photoreceptors in the human eye (Lucas et al. 2014). Moreover, the roughness or irregularity of material surfaces, which are difficult to measure with devices, can be estimated through appearance-driven assessments based

on human observation (Jakubiec 2022; Jones and Reinhart 2017).

In this research, we employ the ARAD_1K dataset (Arad et al. 2022), captured by a hyperspectral camera, as the training data for our recovery network, $S(x)$. To refine the precision of the recovered hyperspectral images and incorporate human observations, we utilise the spectral and observation measurements in the spectraldb (Jakubiec 2022), acquired from a spectrophotometer, as a correction reference.

Hyperspectral Image Recovery Methods

Early attempts to recover hyperspectral images rely on sparse coding methods, such as manifold representation, which embeds high-dimensional spectral information into low-dimensional representations (Li, Huang, and Zhang 2020; Jia et al. 2017). Recent network-based methods investigate network modules that learn both spatial and spectral features (Cai et al. 2022b; Hu et al. 2022). While these methods have achieved accurate spectral recoveries, the application of hyperspectral images is still limited by the lack of annotated hyperspectral image datasets with semantic labels. Despite advancements in solving the spectral recovery challenge for geoscience applications such as aerial image dehazing, the challenge remains a topic of ongoing research for daily images (Mehta et al. 2021; Cai et al. 2022a; Arad et al. 2022). In this paper, we investigate how to apply hyperspectral recovery methods to existing material segmentation datasets. The proposed method can also be applied to other tasks without much modification.

Methodology

The proposed MatSpectNet aims to tackle the material segmentation task by utilising the discriminatory information from reconstructed hyperspectral images. However, the lack of open-access datasets with corresponding hyperspectral images presents an additional challenge for the material segmentation task. To address this, we introduce a physically-constrained spectral recovery architecture and employ a domain-aware training approach (illustrated in Figure 1, (a)) to incorporate hyperspectral information into the material segmentation task. The recovered hyperspectral images are then processed using interpretable spectral filters and combined with other observations such as roughness to improve the segmentation quality (shown in Figure 1, (b)).

Physically-Constrained Spectral Recovery

The spectral recovery network learns the transformation from an sRGB image $x \in \mathcal{X}$ to its corresponding hyperspectral image $\hat{h} \in \mathcal{H}$ via $S : \mathcal{X} \rightarrow \mathcal{H}$ (Cai et al. 2022b; Li et al. 2022a; Agarla et al. 2022; Arad et al. 2022). However, evaluating the quality of reconstructed hyperspectral images is challenging due to the absence of measured hyperspectral images in material datasets. To address this issue, we introduce an RGB transformation network $R : \mathcal{H} \rightarrow \mathcal{X}$ that maps the reconstructed hyperspectral image \hat{h} back to the corresponding sRGB image, as shown in Figure 2. We select the best parameters $\theta^* = \arg \min_{\theta} L_{trans}$ by monitoring the loss term for the material datasets:

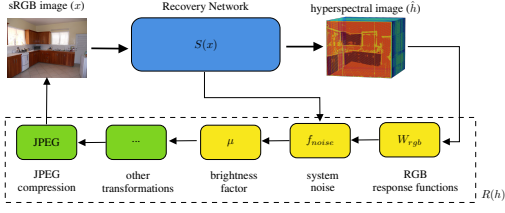


Figure 2: The learnable components in the RGB transformation network, $R(h)$, which models the physical camera. Networks and the yellow components model the green components are modelled by explicit equations.

$$L_{trans} = L_{MSE}(x, R(S_\theta(x))) \quad (1)$$

To recover accurate hyperspectral images for material datasets by minimizing the transformation loss, the design of $R(h)$ must reflect the physical relationship of the RGB and hyperspectral image pair. Hence, a simple network, as used in previous works such as (Mehta et al. 2021), is not sufficient. To address this, $R(h)$ explicitly incorporates the physical RGB camera model including response functions, brightness, and system noise, as shown in Equation 2:

$$R(h) = f_{jpeg}(\mu f_{noise}(W_{rgb}h)) \quad (2)$$

where the hyperspectral image $h \in \mathbb{R}^{n.bands \times H \times W}$ and the RGB response functions are formatted as a matrix $W_{rgb} \in \mathbb{R}^{3 \times n.bands}$. The camera noise is included by the function f_{noise} , and μ is the brightness factor. Here, $n.bands$ is the number of spectra bands sampled by the response functions. The function f_{jpeg} models the in-camera processing and compression noise introduced by the JPEG compression algorithm. All components are trainable in Figure 2 and will be explained in the following paragraphs.

RGB Response Functions. All digital light sensors exhibit varying sensitivity to different wavelength ranges of light due to their spectral response functions (Tropp 2017). Specifically, trichromatic cameras or three-colour image sensors, inspired by human colour perception, have unique spectral response functions in their red (R), green (G), and blue (B) channels based on the tristimulus theory (Smithson 2005). That is to say, if we know the measurement of the spectral reflection h and the response matrix W_{rgb} , sampled at the same bands, the noiseless RGB image rgb_{clean} can be obtained as $W_{rgb}h$, on the condition that h is properly calibrated (Ji et al. 2021; Behmann et al. 2018). However, the RGB values are not consistent across various camera models, even under the same capturing conditions. This is because each model of three-colour image sensors responds differently to light due to their unique RGB spectral response functions. Hence, the RGB values are device-specific and not interchangeable among different camera models.

In order to handle images taken by different camera models (Schwartz and Nishino 2020; Bell et al. 2015, 2013), we propose to learn the sensitivity displacement $\Delta band_i$ at each spectral band i compared with standard response functions based on the input sRGB image, as depicted in

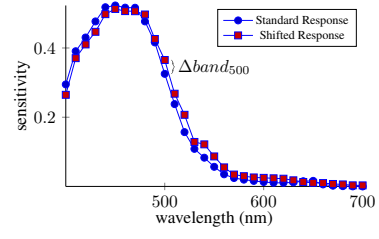


Figure 3: The illustration of the predicted band shift for the blue channel response curve.

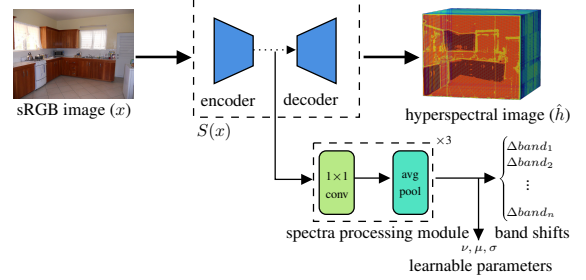


Figure 4: The network architecture to predict the learnable parameters and band shifts.

Figure 3. The standard response curves are sourced from the ARAD_1K dataset, which is based on physical measurements of a Basler Ace 2 camera (Arad et al. 2022). To learn the sensitivity displacement, we redesigned the spectral recovery network $S(x)$, which obeys the encoder-decoder architecture, by attaching one auxiliary path to the encoder. As shown in Figure 4, the encoder output is processed with the repetitive spectra processing module comprising 1×1 convolutional kernels and average pooling. The 1×1 convolutional kernel is responsible to learn from the channel information since the band difference is applied to each pixel individually. The average pooling downsamples the feature map to correct the prediction. Moreover, the response curves should learn from long, middle, and short wavelength regions for R, G, and B channels respectively. To keep maintain the functionality of the response curves, the band differences are aggregated as a loss term L_{band} :

$$L_{band} = \sum_{r,g,b} \sum_{\lambda} band_{\lambda|r,g,b} \times ||\Delta band_{\lambda|r,g,b}|| \quad (3)$$

where $band_{\lambda}$ is sampled from the standard response curve at wavelength λ for channel R or G or B. In this way, the highly sensitive region incurs severe penalties, causing its displacement $\Delta band_{\lambda}$ to be zero and preserving its functionality. In our experiment, the MST++(Cai et al. 2022b) is chosen to be our spectral recovery network $S(x)$ and the spectra processing module in Figure 4 is repeated three times with channel numbers 124, 62, 31+3 where 31 of them is the number of spectra band sampled between 400nm and 700nm with step 10nm, and the other 3 scalars are the noise parameters and brightness factor explained in following sections.

Camera System Noise and Brightness. Since the hyperspectral image h in the ARAD_1K dataset is calibrated with

white and dark reference samples to measure the actual reflectance rather than signal intensity, the recovered hyperspectral image \hat{h} is projected into noiseless RGB rgb_{clean} by $W_{rgb}\hat{h}$. However, for realistic cameras, the camera system noise caused by unwanted variations in the signals produced by the image sensor and processing circuitry can reduce the image quality, particularly in low light conditions or high ISO settings (Baxter and Murray 2012; Shin et al. 2019; Park, Kang, and Lee 2020). Camera system noise can be categorized into several types, including thermal noise caused by random fluctuations in the electrical charge generated by the image sensor due to heat (Berthelon et al. 2018), and shot noise caused by the random nature of the way light interacts with the image sensor (Roussel, Boffety, and Goudail 2018). To address the camera system noise, we simulate camera system noise using parameterised probability models.

Since thermal noise is a form of Gaussian noise, it can be modelled with zero-mean normal distribution $N(0, \sigma)$ where the standard variance σ is considered as the noise level (Denk and Winkler 2007; Chen 2021). As for the shot noise, it arises due to the random nature of the arrival times of particles such as photons at the sensor, hence it can be modelled with Poisson distribution (Roussel, Boffety, and Goudail 2018; Arad et al. 2022) $P(\nu)$ where ν is the noise level which is proportional to the intensity of the incoming light. In summary, the noisy RGB can be represented as:

$$rgb_{noisy} = \mu P((N(0, \sigma) + rgb_{clean}) \times \nu) / \nu \quad (4)$$

where the brightness factor μ adjusts the intensity of the image with the average scene brightness assumption. The noise level ν, σ are tuned and justified in Section C.2 in the supplementary material. In practice, the uniform brightness factor is redundant when the ground truth images and recovered images are normalised into the range $[0, 1]$. The comparison between using $[0, 1]$ normalisation and using brightness factor is in Section C.1 in the supplementary material.

Other Components and Compression Noise. In a typical in-camera processing pipeline, the final sRGB image is derived through various processing steps from the initial noisy raw image rgb_{noisy} . These steps typically involve operations such as white balance, colour manipulation (Tseng et al. 2022), gamma correction, and JPEG compression (Prakash et al. 2022). While the sRGB gamma correction follows a known equation and JPEG compression can be approximated mathematically with differentiable operations (Wang et al. 2022; Mishra, Singh, and Singh 2022; Shin and Song 2017), the specific image style configurations for colour manipulation vary across different camera models and are often intricate and proprietary. To avoid the explicit modelling of these camera-specific components applied to the noisy RGB images, this section proposes a network that encompasses the effects of in-camera processing and the noise induced by JPEG compression. This approach is achieved through the integration of two basic Swin transformer layers (Liu et al. 2021b,a) to post-process the noisy image. The basic Swin layer consists of a window-based self-attention and MLP processing to learn from local regions. The window size is

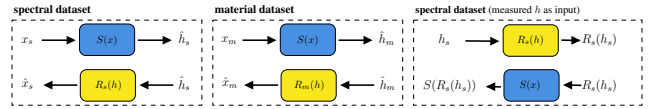


Figure 5: The data flow for spectral as well as material datasets. Specifically, these two datasets share the same $S(x)$ but have their own $R(h)$ to model the cameras.

set to 8, as the JPEG compression algorithm typically applies the 2D discrete cosine transform on 8×8 blocks. This framework enables the generation of final sRGB images that faithfully capture the effects of these in-camera processes, providing a more robust representation of the recovered sRGB images. Though the network architecture may sound simple, the experiments in Section C.3 in the supplementary material show that a simple network is enough to cope with the in-camera processing and compression noise.

Domain-Aware Network Training

The goal of this paper is to employ hyperspectral images for material segmentation. As there are no hyperspectral images in material datasets, we propose to incorporate the spectra dataset ARAD_1K (Arad et al. 2022), which includes pairs of RGB and hyperspectral images, to jointly train the spectral recovery network $S(x)$ and the RGB transformation network $R(h)$ with the material datasets. We denote the samples in the spectral dataset as (x_s, h_s) , and the samples in the material dataset as (x_m) . The total loss is defined as $L_{total} = 10 \times L_{band} + 5 \times (L_{rgb} + L_{spectral}) + 0.5 \times L_{domain}$. Equation 3 has introduced the band loss, while the remaining three terms will be introduced in this section. The domain loss L_{domain} is introduced in Section B.1 in the supplementary material.

RGB Recovery Loss. Ideally, an RGB image passing through $S(x)$ and $R(h)$ should be able to recover itself, as shown in Equation 5.

$$L_{rgb} = L_{trans} + L_{MSE}(x_s, \hat{x}_s) + L_{MSE}(x_s, R_s(h_s)) \quad (5)$$

where \hat{x}_s, \hat{x}_m are recovered RGB images, $R_s(h_s)$ takes the measured hyperspectral image as input, and L_{MSE} is the mean squared error. As shown in Figure 5, x_s and x_m share the same spectra recovery network $S(x)$. As for the RGB transformation networks $R_s(h)$ and $R_m(h)$, these two datasets have their own trainable parameters since the RGB images are taken by different cameras.

Spectral Recovery Loss. To calculate the spectral recovery loss term $L_{spectral}$, we compare the recovered hyperspectral image \hat{h}_s with its ground truth h_s , using the mean relative absolute error (L_{MRAE}) (Arad et al. 2022):

$$L_{spectral} = L_{MRAE}(h_s, \hat{h}_s) + L_{MRAE}(h_s, S(R_s(h_s))) \quad (6)$$

The two terms correspond to the left and right parts of Figure 5. The second term $S(R_s(h_s))$ reverses the order of

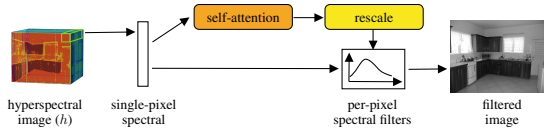


Figure 6: The network architecture to learn filters to aggregate spectra information.

operations in Figure 5 to ensure that the networks $S(x)$ and $R(h)$ are order-irrelevant. Moreover, this term also confirms that the recovered RGB image can be successfully transformed back to the original hyperspectral image.

Interpretable Hyperspectral Processing

The recovery of hyperspectral images opens up the possibility of understanding the contribution of each wavelength to the material segmentation task. This information is useful for modifying camera response curves to generate task-specific images (Saragadam and Sankaranarayanan 2020). To facilitate this, we propose a wavelength-wise self-attention module, named 'spectral attention', which processes the hyperspectral images using predicted filters that have a similar physical meaning as RGB response curves, as shown in Figure 6. By aggregating the hyperspectral images based on their dependencies at each wavelength, this module can identify the spectral information that is most relevant to the task at hand. More detail is in Section D.2 in the supplementary material.

Multi-Modal Fusion

In addition to the spectral information learned from the ARAD_1K dataset, we also want to incorporate human material observations from the spectraldb dataset into the segmentation process. To query the observations, we use the per-pixel spectral measurements s as the bridge to link these two datasets. It is worth noting that the spectral camera and spectrophotometer have different measurement precisions, despite measuring the same physical property. Therefore, in this work, we compare the difference with the spectra shape matrix S of the spectra measurements. The matrix element S_{λ_a, λ_b} is defined in Equation 7:

$$S_{\lambda_a, \lambda_b} = |s_{\lambda_a} - s_{\lambda_b}| \quad (7)$$

where λ_a and λ_b are the wavelength bands within the range [400nm, 700nm]. We construct the spectra shape matrix for both the recovered hyperspectral images as well as the spectraldb measurements (Jakubiec 2022), which contains multiple spectra measurements indexed by k .

As shown in Figure 7, for each pixel i, j in the hyperspectral image, we find the matched measurement $S_k^* = \arg \min_{S_k} \|S[i, j] - S_k\|_2$ with the L_2 distance. Then the corresponding observations including reflectance, specularity and roughness are appended to pixel i, j of the recovered hyperspectral image. The queried observations together with the filtered features are passed into MLP to extract material features, as shown in Figure 1. The way we generate the final material prediction is described in Section B.5 in the supplementary material.

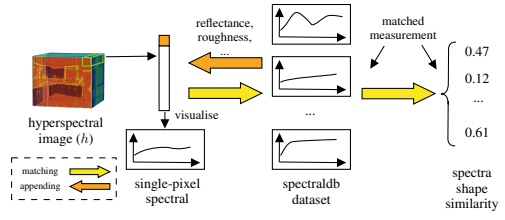


Figure 7: The mechanism to find the matched sample in the spectraldb dataset.

Experiments

In this paper, we assess the performance of our network on two material datasets, namely the LMD dataset (Schwartz 2018; Schwartz and Nishino 2020) and the OpenSurfaces dataset (Bell et al. 2013), using the evaluation metrics reported in (Heng et al. 2022a). The MatSpectNet is trained for 400 epochs with 8 NVIDIA GeForce RTX 3090 GPUs. The training configurations are in Section B, the spectral recovery experiments are in Section C, and the additional analysis is in Section D in the supplementary material.

Quantitative Evaluation

Table 1 presents numerical evaluations of seven networks. Our MatSpectNet outperforms all other compared networks on both datasets. Specifically, on the LMD dataset, our MatSpectNet achieves the highest per-pixel averaged accuracy (Pixel Acc) of 88.24% and mean-class accuracy (Mean Acc) of 83.82%. Compared to the second-best performing network, DBAT (Heng et al. 2022a), the MatSpectNet shows improvements of 1.60% and 3.42% for Pixel Acc and Mean Acc, respectively. On the OpenSurfaces dataset, the MatSpectNet also achieves the best performance with accuracy scores of 87.13% and 71.29% for Pixel Acc and Mean Acc, respectively. The corresponding improvements compared to the second-best scores are 0.99% and 0.86%. In particular, for the LMD dataset, the higher improvement in Mean Acc and lower improvement in Pixel Acc indicate that our MatSpectNet improves the performance for hard-to-recognize material categories compared to other networks, suggesting that hyperspectral information can provide reliable material features. The detailed per-category performance is reported in the supplementary material.

Qualitative Evaluation

The segmented images are displayed in Figure 8. Despite the sparsely labelled ground truth (Heng et al. 2022b,a; Schwartz and Nishino 2020), our MatSpectNet is the only model that can accurately classify nearly all the pixels belonging to the stone wall, even those under bright lighting conditions. This suggests that the calibrated spectral information can boost network performance under varying illumination conditions, as compared to other purely image-based networks.

However, we also noticed that the material labels defined in the LMD dataset lack the ability to fully describe indoor scenes in a dense manner. Furthermore, the similarity in appearance of different materials makes the segmentation task

Datasets Architecture	LMD		OpenSurfaces			—		
	Pixel Acc (%)	Mean Acc (%)	Pixel Acc (%)	Mean Acc (%)	mIoU (%)	#params (M)	#flops (G)	FPS
ResNeSt-101 (Zhang et al. 2022)	82.45 \pm 0.20	75.31 \pm 0.29	85.10	67.13	55.32	48.84	63.39	25.57
EfficientNet-b5 (Tan and Le 2019)	83.17 \pm 0.06	76.91 \pm 0.06	84.63	65.47	53.25	30.17	20.5	27.00
Swin-t (Liu et al. 2021b)	84.70 \pm 0.26	79.06 \pm 0.46	86.19	69.41	57.71	29.52	34.25	33.94
CAM-SegNet-DBA (Heng et al. 2022a)	86.12 \pm 0.15	79.85 \pm 0.28	86.64	69.92	58.18	68.58	60.83	17.79
DBAT (Heng et al. 2022a)	86.85 \pm 0.08	81.05 \pm 0.28	86.28	70.68	58.08	56.03	41.23	27.44
MatSpectNet	88.24 \pm 0.10	83.82 \pm 0.23	87.13	71.29	58.92	57.7	42.16	26.83

Table 1: The performance (Heng et al. 2022b) reported on the LMD and the OpenSurfaces. The FPS value of MatSpectNet is calculated by processing 1000 images with one NVIDIA 3090. The uncertainty evaluation is reported across five trainings.

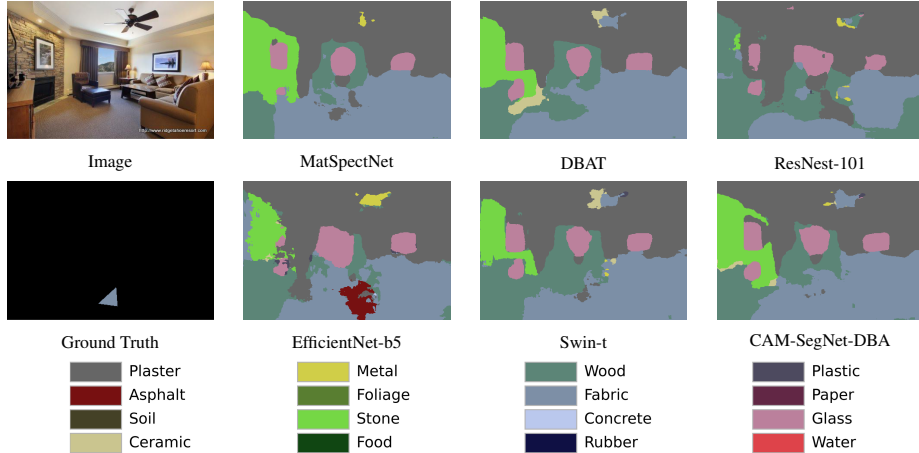


Figure 8: Predicted segmentation of one living room image.

Methods	Regularised Spectral Recovery	Domain Alignment	Multi-Modal Fusion
Network 1			
Network 2	✓		
Network 3	✓	✓	
MatSpectNet	✓	✓	✓

Table 2: The network variations and the corresponding enabled components.

n_filters	4	8	12	16
Network 1	86.73/80.91	86.55/80.14	86.94/81.13	87.08/81.20
Network 2	86.93/81.41	87.17/81.74	87.69/81.92	87.10/81.63
Network 3	87.16/82.88	87.22/82.93	87.46/81.71	87.54/82.36
MatSpectNet	87.95/83.17	87.66/83.14	88.24/83.82	88.07/83.52

Table 3: The network performance for each variation against four filter number choices.

challenging to solve with RGB images. As spectral information is independent of visual appearance, we believe that hyperspectral reconstruction could be a potential solution to overcome the limitation of sparse labeling for pixels that cannot be adequately described by the given labels.

Ablation Study

In this section, we assess the impact of each component of the proposed MatSpectNet by introducing three additional models of increasing complexity, as shown in Table 2. For each model, we adjust the number of filters in the interpretable hyperspectral processing module and report the corresponding (Pixel Acc/Mean Acc) results on the LMD

dataset in Table 3.

Regularised Spectral Recovery. Network 1 utilises a pre-trained spectral recovery network to generate the hyperspectral images. However, since the network is not specifically tuned for the material datasets, the network trained on the ARAD_1K dataset is not generalisable, and the network performance is hardly improved. In contrast, when the spectral recovery network is equipped with the physically-constrained RGB transformation network, Network 2 achieves up to 0.75 p.p. improvement in Pixel Acc and 1.60 p.p. improvement in Mean Acc¹. However, the training process does not guarantee an increase in network performance, as evidenced by the results for filter number 8.

Domain Alignment. The domain alignment strategy is designed to learn generalisable features for material datasets without training samples. The reported evaluations show that network 3 improves network performance for all filter choices, indicating that the features extracted by the spectral recovery network are well-tuned for material datasets.

Multi-Modal Fusion. The spectradb dataset provides measurements and observations that can help reduce network uncertainty in identifying materials. As shown in Table 3, the MatSpectNet achieves the best performance with an improvement of 0.78 p.p./2.11 p.p. when the filter number is set to 12 compared with Network 3. The significant increase indicates that human observations, such as roughness, can reliably differentiate between different materials.

¹p.p. means percentage point

References

- Agarla, M.; Bianco, S.; Buzzelli, M.; Celona, L.; and Schettini, R. 2022. Fast-n-squeeze: towards real-time spectral reconstruction from rgb images. In *Proceedings of the IEEE/CVF Conference on Computer Vision and Pattern Recognition*, 1132–1139.
- Arad, B.; Timofte, R.; Yahel, R.; Morag, N.; Bernat, A.; Cai, Y.; Lin, J.; Lin, Z.; Wang, H.; Zhang, Y.; et al. 2022. NTIRE 2022 Spectral Recovery Challenge and Data Set. In *Proceedings of the IEEE/CVF Conference on Computer Vision and Pattern Recognition*, 863–881.
- Baxter, D. J.; and Murray, A. 2012. Calibration and adaptation of ISO visual noise for I3A's Camera Phone Image Quality initiative. In *Image Quality and System Performance IX*, volume 8293, 21–34. SPIE.
- Behmann, J.; Acebron, K.; Emin, D.; Bennertz, S.; Matsubara, S.; Thomas, S.; Bohnenkamp, D.; Kuska, M. T.; Jussila, J.; Salo, H.; et al. 2018. Specim IQ: Evaluation of a new, miniaturized handheld hyperspectral camera and its application for plant phenotyping and disease detection. *Sensors*, 18(2): 441.
- Bell, S.; Upchurch, P.; Snavely, N.; and Bala, K. 2013. OpenSurfaces: A Richly Annotated Catalog of Surface Appearance. *ACM Trans. on Graphics (SIGGRAPH)*, 32(4).
- Bell, S.; Upchurch, P.; Snavely, N.; and Bala, K. 2015. Material Recognition in the Wild with the Materials in Context Database. *Computer Vision and Pattern Recognition (CVPR)*.
- Berthelon, X.; Chenegros, G.; Finateu, T.; Ieng, S.-H.; and Benosman, R. 2018. Effects of cooling on the SNR and contrast detection of a low-light event-based camera. *IEEE transactions on biomedical circuits and systems*, 12(6): 1467–1474.
- Cai, Y.; Lin, J.; Hu, X.; Wang, H.; Yuan, X.; Zhang, Y.; Timofte, R.; and Van Gool, L. 2022a. Coarse-to-fine sparse transformer for hyperspectral image reconstruction. In *Computer Vision—ECCV 2022: 17th European Conference, Tel Aviv, Israel, October 23–27, 2022, Proceedings, Part XVII*, 686–704. Springer.
- Cai, Y.; Lin, J.; Lin, Z.; Wang, H.; Zhang, Y.; Pfister, H.; Timofte, R.; and Van Gool, L. 2022b. Mst++: Multi-stage spectral-wise transformer for efficient spectral reconstruction. In *Proceedings of the IEEE/CVF Conference on Computer Vision and Pattern Recognition*, 745–755.
- Chen, C.-H. 2021. Thermal noise measurement and characterization for modern semiconductor devices. *IEEE Instrumentation & Measurement Magazine*, 24(2): 60–71.
- Colthup, N. B.; Daly, L. H.; and Wiberley, S. E. 1990. Front Matter. In *Introduction to Infrared and Raman Spectroscopy (Third Edition)*. San Diego: Academic Press, third edition edition. ISBN 978-0-12-182554-6.
- Denk, G.; and Winkler, R. 2007. Modelling and simulation of transient noise in circuit simulation. *Mathematical and Computer Modelling of Dynamical Systems*, 13(4): 383–394.
- Heng, Y.; Wu, Y.; Dasmahapatra, S.; and Kim, H. 2022a. Enhancing Material Features Using Dynamic Backward Attention on Cross-Resolution Patches. In *33rd British Machine Vision Conference 2022, BMVC 2022, London, UK, November 21-24, 2022*. BMVA Press.
- Heng, Y.; Wu, Y.; Kim, H.; and Dasmahapatra, S. 2022b. CAM-SegNet: A Context-Aware Dense Material Segmentation Network for Sparsely Labelled Datasets. In *17th International Conference on Computer Vision Theory and Applications (VISAPP)*, volume 5, 190–201.
- Hu, X.; Cai, Y.; Lin, J.; Wang, H.; Yuan, X.; Zhang, Y.; Timofte, R.; and Van Gool, L. 2022. Hdnet: High-resolution dual-domain learning for spectral compressive imaging. In *Proceedings of the IEEE/CVF Conference on Computer Vision and Pattern Recognition*, 17542–17551.
- Jain, C.; Bhargava, A.; Gupta, S.; Rath, R.; Nagpal, A.; and Kumar, P. 2013. Spectrophotometric evaluation of the color changes of different feldspathic porcelains after exposure to commonly consumed beverages. *European Journal of Dentistry*, 7(02): 172–180.
- Jakubiec, J. A. 2016. Building a database of opaque materials for lighting simulation. In *PLEA 2016—Cities, Buildings, People: Towards Regenerative Environments*,. *Proceedings of the 32nd International Conference on Passive and Low Energy Architecture*.
- Jakubiec, J. A. 2022. Data-Driven Selection of Typical Opaque Material Reflectances for Lighting Simulation. *LEUKOS*, 1–14.
- Ji, Y.; Kwak, Y.; Park, S. M.; and Kim, Y. L. 2021. Compressive recovery of smartphone RGB spectral sensitivity functions. *Optics Express*, 29(8): 11947–11961.
- Jia, Y.; Zheng, Y.; Gu, L.; Subpa-Asa, A.; Lam, A.; Sato, Y.; and Sato, I. 2017. From RGB to spectrum for natural scenes via manifold-based mapping. In *Proceedings of the IEEE international conference on computer vision*, 4705–4713.
- Jones, N. L.; and Reinhart, C. F. 2017. Experimental validation of ray tracing as a means of image-based visual discomfort prediction. *Building and Environment*, 113: 131–150.
- Kalman, L. S.; and Bassett III, E. M. 1997. Classification and material identification in an urban environment using HYDICE hyperspectral data. In *Imaging Spectrometry III*, volume 3118, 57–68. SPIE.
- Li, J.; Du, S.; Wu, C.; Leng, Y.; Song, R.; and Li, Y. 2022a. Drcr net: Dense residual channel re-calibration network with non-local purification for spectral super resolution. In *Proceedings of the IEEE/CVF Conference on Computer Vision and Pattern Recognition*, 1259–1268.
- Li, M.; Liu, Y.; Xue, G.; Huang, Y.; and Yang, G. 2022b. Exploring the Relationship between Center and Neighborhoods: Central Vector oriented Self-Similarity Network for Hyperspectral Image Classification. *IEEE Transactions on Circuits and Systems for Video Technology*.
- Li, Z.; Huang, H.; and Zhang, Z. 2020. Deep manifold reconstruction neural network for hyperspectral image classification. *IEEE Geoscience and Remote Sensing Letters*, 19: 1–5.

- Liang, Y.; Wakaki, R.; Nobuhara, S.; and Nishino, K. 2022. Multimodal Material Segmentation. In *Proceedings of the IEEE/CVF Conference on Computer Vision and Pattern Recognition*, 19800–19808.
- Lichtman, J. W.; and Conchello, J.-A. 2005. Fluorescence microscopy. *Nature methods*, 2(12): 910–919.
- Liu, S.; Marinelli, D.; Bruzzone, L.; and Bovolo, F. 2019. A review of change detection in multitemporal hyperspectral images: Current techniques, applications, and challenges. *IEEE Geoscience and Remote Sensing Magazine*, 7(2): 140–158.
- Liu, Z.; Hu, H.; Lin, Y.; Yao, Z.; Xie, Z.; Wei, Y.; Ning, J.; Cao, Y.; Zhang, Z.; Dong, L.; et al. 2021a. Swin Transformer V2: Scaling Up Capacity and Resolution. *arXiv preprint arXiv:2111.09883*.
- Liu, Z.; Lin, Y.; Cao, Y.; Hu, H.; Wei, Y.; Zhang, Z.; Lin, S.; and Guo, B. 2021b. Swin transformer: Hierarchical vision transformer using shifted windows. In *Proceedings of the IEEE/CVF International Conference on Computer Vision*, 10012–10022.
- Lucas, R. J.; Peirson, S. N.; Berson, D. M.; Brown, T. M.; Cooper, H. M.; Czeisler, C. A.; Figueiro, M. G.; Gamlin, P. D.; Lockley, S. W.; O’Hagan, J. B.; et al. 2014. Measuring and using light in the melanopsin age. *Trends in neurosciences*, 37(1): 1–9.
- Magnusson, M.; Sigurdsson, J.; Armansson, S. E.; Ulfarsson, M. O.; Deborah, H.; and Sveinsson, J. R. 2020. Creating RGB images from hyperspectral images using a color matching function. In *IGARSS 2020-2020 IEEE International Geoscience and Remote Sensing Symposium*, 2045–2048. IEEE.
- Mao, S.; Ji, M.; Wang, B.; Dai, Q.; and Fang, L. 2022. Surface material perception through multimodal learning. *IEEE Journal of Selected Topics in Signal Processing*, 16(4): 843–853.
- Mehta, A.; Sinha, H.; Mandal, M.; and Narang, P. 2021. Domain-aware unsupervised hyperspectral reconstruction for aerial image dehazing. In *Proceedings of the IEEE/CVF winter conference on applications of computer vision*, 413–422.
- Mishra, D.; Singh, S. K.; and Singh, R. K. 2022. Deep architectures for image compression: a critical review. *Signal Processing*, 191: 108346.
- Park, C. R.; Kang, S.-H.; and Lee, Y. 2020. Median modified wiener filter for improving the image quality of gamma camera images. *Nuclear Engineering and Technology*, 52(10): 2328–2333.
- Prakash, D. C.; Narayanan, R.; Ganesh, N.; Ramachandran, M.; Chinnasami, S.; and Rajeshwari, R. 2022. A study on image processing with data analysis. In *AIP Conference Proceedings*, volume 2393, 020225. AIP Publishing LLC.
- Roussel, S.; Boffety, M.; and Goudail, F. 2018. Polarimetric precision of micropolarizer grid-based camera in the presence of additive and Poisson shot noise. *Optics express*, 26(23): 29968–29982.
- Saragadam, V.; and Sankaranarayanan, A. C. 2020. Programmable spectrometry: per-pixel material classification using learned spectral filters. In *2020 IEEE International Conference on Computational Photography (ICCP)*, 1–10. IEEE.
- Schwartz, G. 2018. *Visual Material Recognition*. Drexel University.
- Schwartz, G.; and Nishino, K. 2016. Material Recognition from Local Appearance in Global Context. In *Biol. and Artificial Vision (Workshop held in conjunction with ECCV 2016)*.
- Schwartz, G.; and Nishino, K. 2020. Recognizing Material Properties from Images. *IEEE Transactions on Pattern Analysis and Machine Intelligence*, 42(8): 1981–1995.
- Shaikh, M. S.; Jaferzadeh, K.; Thörnberg, B.; and Casselgren, J. 2021. Calibration of a hyper-spectral imaging system using a low-cost reference. *Sensors*, 21(11): 3738.
- Shin, R.; and Song, D. 2017. Jpeg-resistant adversarial images. In *NIPS 2017 Workshop on Machine Learning and Computer Security*, volume 1, 8.
- Shin, U.; Park, J.; Shim, G.; Rameau, F.; and Kweon, I. S. 2019. Camera exposure control for robust robot vision with noise-aware image quality assessment. In *2019 IEEE/RSJ International Conference on Intelligent Robots and Systems (IROS)*, 1165–1172. IEEE.
- Smith, V. C.; and Pokorny, J. 1996. The design and use of a cone chromaticity space: a tutorial. *Color Research & Application*, 21(5): 375–383.
- Smithson, H. E. 2005. Sensory, computational and cognitive components of human colour constancy. *Philosophical Transactions of the Royal Society B: Biological Sciences*, 360(1458): 1329–1346.
- Stuart, M. B.; Davies, M.; Hobbs, M. J.; Pering, T. D.; McGonigle, A. J.; and Willmott, J. R. 2022. High-resolution hyperspectral imaging using low-cost components: Application within environmental monitoring scenarios. *Sensors*, 22(12): 4652.
- Su, S.; Heide, F.; Swanson, R.; Klein, J.; Callenberg, C.; Hullin, M.; and Heidrich, W. 2016. Material classification using raw time-of-flight measurements. In *Proceedings of the IEEE conference on computer vision and pattern recognition*, 3503–3511.
- Tan, M.; and Le, Q. 2019. Efficientnet: Rethinking model scaling for convolutional neural networks. In *International conference on machine learning*, 6105–6114. PMLR.
- Tropp, J. A. 2017. A mathematical introduction to compressive sensing [Book Review]. *Bulletin of the American Mathematical Society*, 54(1): 151–165.
- Tseng, E.; Zhang, Y.; Jebe, L.; Zhang, X.; Xia, Z.; Fan, Y.; Heide, F.; and Chen, J. 2022. Neural Photo-Finishing. *ACM Transactions on Graphics (TOG)*, 41(6): 1–15.
- Wang, D.; Yang, W.; Hu, Y.; and Liu, J. 2022. Neural data-dependent transform for learned image compression. In *Proceedings of the IEEE/CVF Conference on Computer Vision and Pattern Recognition*, 17379–17388.

Wu, Y.; Heng, Y.; Niranjana, M.; and Kim, H. 2021. Depth estimation from a single omnidirectional image using domain adaptation. In *European Conference on Visual Media Production*, 1–9.

Xue, Z.; Zhang, M.; Liu, Y.; and Du, P. 2021. Attention-based second-order pooling network for hyperspectral image classification. *IEEE Transactions on Geoscience and Remote Sensing*, 59(11): 9600–9615.

Zhang, C.; Marty, J.; Maynadier, A.; Chaudet, P.; Réthoré, J.; and Baietto, M.-C. 2019. An innovative technique for real-time adjusting exposure time of silicon-based camera to get stable gray level images with temperature evolution. *Mechanical Systems and Signal Processing*, 122: 419–432.

Zhang, H.; Wu, C.; Zhang, Z.; Zhu, Y.; Lin, H.; Zhang, Z.; Sun, Y.; He, T.; Mueller, J.; Manmatha, R.; et al. 2022. Resnest: Split-attention networks. In *Proceedings of the IEEE/CVF Conference on Computer Vision and Pattern Recognition*, 2736–2746.

Zhong, Y.; Wang, X.; Zhao, L.; Feng, R.; Zhang, L.; and Xu, Y. 2016. Blind spectral unmixing based on sparse component analysis for hyperspectral remote sensing imagery. *ISPRS Journal of Photogrammetry and Remote Sensing*, 119: 49–63.